JOURNAL OF SPACECRAFT AND ROCKETS
Vol. 31, No. 4, July–August 1994

Euler and Navier-Stokes Solutions for Supersonic Flow Around A Complex Missile

Th. Streit*
Deutsche Forschungsanstalt fur Luft und Raumfahrt (DLR), D-38108 Braunschweig, Germany

The numerical solution of the Euler and Navier-Stokes system of equations and experimental data for the supersonic flow around a complex missile configuration are compared. The Euler and Navier-Stokes equations are solved with the DLR finite-volume method CEVCATS using multiblock mesh structure and multigrid acceleration technique. The numerical solution of the flow equations for this missile with eight fins has provided a flow with a rich vortex structure and manifold three-dimensional effects. The aerodynamic coefficients for normal-force and pitching moment obtained with the Euler solution are in good agreement with experimental values. Therefore, the position of the aerodynamic center is well-predicted by the inviscid solution. However for the flow close to the surface a Navier-Stokes solution is required to obtain agreement with the experimental results.

Nomenclature

C_{mb} = global pitching moment coefficient
C_p = pressure coefficient
C_{xa} = global drag coefficient
C_{zb} = global normal-force coefficient
$\overline{D}$ = maximum diameter of missile body, in SI units
E = total energy, normalized by $\overline{p}_\infty/\overline{\rho}_\infty$
H = total enthalpy, normalized by $\overline{p}_\infty/\overline{\rho}_\infty$
L = missile length, normalized by $\overline{D}$
M = Mach number
Pr = Prandtl number
p = static pressure, normalized by $\overline{p}_\infty$
q = velocity vector, in units of $\sqrt{\overline{p}_\infty/\overline{\rho}_\infty}$
$Re_{\overline{D}}$ = Reynolds number, $\overline{\rho}_\infty \overline{q}_\infty \overline{D}/\overline{\mu}_\infty$
T = temperature, normalized by $\overline{T}_\infty$
u, v, w = Cartesian velocity components, normalized by $\sqrt{\overline{p}_\infty/\overline{\rho}_\infty}$
x, y, z = Cartesian coordinates, normalized by $\overline{D}$, also denoted as x_1, x_2, x_3
α = angle of attack
ρ = density, normalized by $\overline{\rho}_\infty$
γ = ratio of specific heats, 1.4
ζ, η, ξ = curvilinear coordinates
Φ_x = angle around longitudinal axis

Subscripts

a = aerodynamic system
b = body-fixed system
i, j, k = discretization index, in the ζ, η, ξ directions
inv = inviscid
l = laminar
ref = reference
t = turbulent
tr = transition
vis = viscous
w = to denote quantities defined at solid wall boundary
∞ = condition of freestream

Superscripts

Base = to denote quantities defined at the base
( ) = (overbar) used to denote dimesional quantities

Received Jan 2, 1993; revision received May 10, 1993; accepted for publication May 11, 1993.

*Research Scientist, DLR Institute of Design-Aerodynamics, Aerothermodynamics Branch.

Introduction

FOR complex missile configurations flying at supersonic and hypersonic speeds one cannot rely completely on data bases or preliminary design tools to predict aerodymanic coefficients and assure stability. In contrast to these methods, an inviscid modeling has the advantage that the solution of the Euler equations captures the characteristic nonlinear features of supersonic flow around a missile.[1-4] These features are: the bow shock, vortices on the leeside of the missile body as well as on the leeside of the fins, crossflow shocks, and interaction of shocks. However a comparison with experimental values shows discrepancies in the position of separation lines as well as in the predicted strength for the vortices at the leeside of the body.[1,3] Nevertheless, inviscid flow computations with crossflow separation modeling[1,4] lead to an improvement of the results.

With a larger degree of body slenderness L/D the boundary layer becomes so important that without a viscous modeling even lift and moment coefficients are not accurately predicted for small incidence flow.[5] Viscous calculations have been done using parabolized Navier-Stokes and Navier-Stokes solvers.[6,7]

With the implementation of multigrid schemes into the DLR multiple block code CEVCATS[8] for supersonic and hypersonic speeds, the code can now be used for viscous problems around complex configurations at a reasonable computing cost. This code is used to numerically obtain the solution of the Euler and Navier-Stokes equations for a missile configuration with eight fins at the rear assembly. At large incidence angle, the resulting flow shows crossflow separations on the forebody and fins with a rich vortex structure.

Experimental data is available from measurements in the DLR Trisonic Wind Tunnel Cologne (TMK) wind tunnel. The experimental data includes: global force and moment measurements for $M_\infty = 3.0$ and 4.2 with $|\alpha| \leq 8.5$ deg, pressure distributions measured at two crossflow planes, and an oil flow picture for $M_\infty = 3.0$ and $\alpha = 8.5$ deg. This experimental data is compared with the numerical results for the Euler and Navier-Stokes equation.

Governing Equations

The three-dimensional, mass-averaged Navier-Stokes equations for unsteady compressible flows may be written in integral form using a Cartesian coordinate system as

$$\iiint_V \frac{\partial}{\partial t} \boldsymbol{W}\, dV = -\iint_{\partial V} \bar{\bar{F}} \cdot \boldsymbol{n}\, dS \tag{1}$$

where

$$\boldsymbol{W} = (\rho, \rho u, \rho v, \rho w, \rho E)^T \tag{2}$$

is the vector of conserved quantities. V denotes an arbitrary control volume fixed in time and space and ∂V is its closed boundary with $\boldsymbol{n}$ being its outward facing normal. $\bar{\bar{F}}$ represents the tensor of flux density, which is composed of an convective part $\bar{\bar{F}}_c$ and a viscous part $\bar{\bar{F}}_v$, i.e.,

$$\bar{\bar{F}} = \bar{\bar{F}}_c - \bar{\bar{F}}_v \tag{3}$$

$$\bar{\bar{F}}_c = \begin{pmatrix} \rho \boldsymbol{q} \\ \rho u \boldsymbol{q} + p \boldsymbol{i}_x \\ \rho v \boldsymbol{q} + p \boldsymbol{i}_y \\ \rho w \boldsymbol{q} + p \boldsymbol{i}_z \\ \rho H \boldsymbol{q} \end{pmatrix}, \qquad \bar{\bar{F}}_v = \begin{pmatrix} 0 \\ \boldsymbol{i}_x \cdot \bar{\bar{\tau}} \\ \boldsymbol{i}_y \cdot \bar{\bar{\tau}} \\ \boldsymbol{i}_z \cdot \bar{\bar{\tau}} \\ \boldsymbol{q} \cdot \bar{\bar{\tau}} + k \nabla T \end{pmatrix} \tag{4}$$

The velocity vector $\boldsymbol{q}$ is given by $\boldsymbol{q} = u\boldsymbol{i}_x + v\boldsymbol{i}_y + w\boldsymbol{i}_z$ with $\boldsymbol{i}_x$, $\boldsymbol{i}_y$, $\boldsymbol{i}_z$ being the unit vectors of the Cartesian coordinate system (also denoted $\boldsymbol{i}_1$, $\boldsymbol{i}_2$, $\boldsymbol{i}_3$). The contribution to the flux density tensor due to the shear stress is expressed in dyadic form and defined as

$$\bar{\bar{\tau}} = \boldsymbol{i}_i \tau_{ij} \boldsymbol{i}_j, \qquad \tau_{ij} = \mu \left(\frac{\partial u_i}{\partial x_j} + \frac{\partial u_j}{\partial x_i} - \frac{2}{3} \delta_{ij} \frac{\partial u_j}{\partial x_i} \right) \tag{5}$$

with μ being the dimensionless viscosity. The total enthalpy H is given by

$$H = E + p/\rho \tag{6}$$

The equation of state for an ideal gas is used to calculate the pressure and temperature in terms of the dependant variables:

$$p = \rho(\gamma - 1)\left(E - \frac{q^2}{2}\right), \qquad T = \frac{p}{\rho} \tag{7}$$

The heat conductivity is given by

$$k = \frac{\gamma}{\gamma - 1} \frac{\mu}{Pr} \tag{8}$$

For laminar flow $\mu = \mu_l$ and the laminar viscosity μ_l is calculated using Sutherlands empirical formula

$$\mu_l = \mu_\infty \left(\frac{\bar{T}}{\bar{T}_\infty} \right)^{3/2} \frac{\bar{T}_\infty + 110}{\bar{T} + 110}, \qquad \mu_\infty = \frac{\gamma^{1/2} M_\infty}{Re_\infty} \tag{9}$$

with $\bar{T}_\infty$, $\bar{T}$ in Kelvin.

Turbulence is taken into account through the introduction of a turbulent viscosity μ_t. For turbulent flow μ is then given by $\mu_l + \mu_t$. In the present work, the turbulence model of Baldwin and Lomax[9] is used. At large incidence onflow the considered configuration shows crossflow separation with vortices at the leeside. Due to a vortex the maximum of vorticity times the distance from the wall is displaced from the boundary layer to the vortex core. Not taking this into account leads to a incorrect value for μ_t. To avoid this the modifications proposed by Degani and Schiff[10] are introduced in the algebraic turbulence model.

Solution Scheme

Spatial Discretization

The numerical approximation of Eq. (1) follows the method of lines which decouples the discretization in space and time. The physical domain around the aerodynamic body is divided into hexahedral cells by the generation of a body-fitted grid. The discrete values of the flow quantities are located at the vertices of the mesh cells. For the flux calculation an auxiliary grid is used which is defined by connecting the cell centers of the original cell. The integral equation (1) is approximated by the spatial discretization

$$V_{i,j,k}\left(\frac{\partial}{\partial t}\boldsymbol{W}_{i,j,k}\right) = -\boldsymbol{R}_{i,j,k} \tag{10}$$

where $V_{i,j,k}$ denotes the volume of the control volume surrounding the grid node (i, j, k). The right-hand side of Eq. (10) represents an approximation of the net flux of mass, momentum, and energy. It is calculated as

$$\boldsymbol{R}_{i,j,k} = \boldsymbol{R}_{i+1/2,j,k} - \boldsymbol{R}_{i-1/2,j,k} + \boldsymbol{R}_{i,j+1/2,k} - \boldsymbol{R}_{i,j-1/2,k} + \boldsymbol{R}_{i,j,k+1/2} - \boldsymbol{R}_{i,j,k-1/2} \tag{11}$$

where the flux through cell face $i + \frac{1}{2}$ can be written in general as

$$\boldsymbol{R}_{i+1/2,j,k} = (\boldsymbol{Q}_c)_{i+1/2,j,k} + \boldsymbol{D}_{i+1/2,j,k} + (\boldsymbol{Q}_v)_{i+1/2,j,k} \tag{12}$$

The first two terms on the right-hand side of Eq. (12) correspond to the approximation of the inviscid flux (convection and pressure) and the third term corresponds to the viscous flux. For the discretization of the viscous fluxes central differences are computed using a local transformation from Cartesian coordinates to the curvilinear coordinates.[11] In this work viscous fluxes are taken into account only in the coordinate direction normal to the body surface (thin-layer approximation). The inviscid flux is discretized with a symmetric approximation of the convective flux represented by $\boldsymbol{Q}_c$. $\boldsymbol{D}$ denotes an operator described by an antidiffusive flux function which adapts the central flux stencil in accordance with local wave propagation theory to that of a second-order accurate, upwind-biased scheme. The second-order upwind scheme used here is based on the total variation Diminishing (TVD) method of Yee and Harten.[12] For a detailed description of the discretization of the terms $(\boldsymbol{Q}_c)_{i+1/2,j,k}$ and $\boldsymbol{D}_{i+1/2,j,k}$ see Ref. 13). Here the modifications introduced for viscous flow are discussed instead.

Yee and Harten's scheme makes use of an entropy function Ψ which prevents the scheme from violating the entropy condition when the wave speeds vanish. The original functional form for Ψ as given by Yee and Harten[12] was redesigned, as was proposed in Ref. 14, to allow viscous flow computations without numerical smearing of the shear layer. Furthermore, it allows the use of mesh cells with high aspect ratios.

Time-Stepping Scheme for Hypersonic Flows

Explicit multistage time-stepping schemes are used for advancing the solution in time. Choosing the number of stages and the stage coefficients allows an optimization of the high-frequency damping properties of the scheme at relatively high Courant numbers. For this work a five-stage scheme with three evaluations of numerical damping terms[14] is used.

Acceleration Techniques for Hypersonic Flows

Convergence rates of explicit time-stepping schemes used for viscous flow computations are usually slow. The reason is the limitation of the time step size by the small cells necessary to resolve thin boundary layers. In addition the computation of high-speed flow requires the implementation of several special features to enhance robustness and to allow the use of acceleration techniques for high-speed flows. A local time step is used at each grid point to advance the solution at the maximum time step allowed by stability considerations. The combined use of a multigrid scheme and implicit residual smoothing with optimized time-stepping coefficients leads to a accelerated reduction of the residual for all its Fourier modes. In the present study the Courant-Friedrichs-Lewy (CFL) number with residual smoothing is CFL = 5, where the explicit stability limit of the five-stage scheme is CFL = 2.4.

The interested reader can find a detailed description for the mentioned acceleration techniques, especialy concerning the introduced modification for viscous hypersonic flow in Refs. 14 and 15.

Boundary Conditions

Generally, three distinct types of boundary equations occur in the numerical scheme of the Navier-Stokes equations. These are the conditions on a solid body, the condition across coordinate cuts, and inflow/outflow conditions in the far field.

Far-field boundaries are implemented using the concept of characteristic variables. In the present work a constant wall temperature T_w is assumed. This, together with the no-slip condition for the solid wall surface and a linear extrapolation of pressure from the next interior grid point fixes all five flow variables at the solid wall. In the case of a slip wall, points at the wall are updated through flux integration like interior points and the wall boundary condition of zero normal velocity is forced by recalculating the velocity components for the wall boundary points.

The CEVCATS code allows the computation of flows with a polar singularity in the nose region. In the case of a pointed nose and supersonic onflow with an attached shock the polar singularity degenerates to a point. Flow variables for this point are updated using a conical boundary condition.

Multiblock Structure

Calculations of viscous flow for complex configurations require a large number of grid points on grid topologies which are determined by the geometrical properties of the solid wall surface and the grid enclosing the far-field boundary. The CEVCATS code is written in a block-structured form which allows calculations of viscous flows for complex configurations with a nearly unrestricted number of grid points on arbitrary grid topologies.[16]

Numerical Results

In this section the model geometry and flow conditions are described first. The grid convergence and convergence of the solution to the steady state is discussed next. Then we will compare the experimental data for the global force and moment aerodynamic coefficients with the numerical results. Next the flowfield will be described using contour plots for Mach number, pressure, and total pressure loss. Then the flow on the surface will be analyzed by comparing the surface streamlines with the skin friction lines on the oil flow picture. The vortex topology related to the identified singular stream lines on the surface is then discussed by showing representations of the velocity vector in crossflow planes. Finally the experimental pressure distributions for the two crossflow planes (one just before the leading edge of the fins and the other in the fin region) are compared with the experimental results.

Geometry and Flow Conditions

The configuration is a projectile with a pointed conical nose followed by an afterbody with a conical flare. Due to the limited fin span, eight fins are placed at the rear part of the afterbody to ensure stability. The fins extend beyond the afterbody. The surface mesh is shown in Fig. 1.

Solutions were obtained for the following flow conditions: $M_\infty = 3.0$ and 4.25, with $\alpha \leq 8$ deg and 5 deg for the inviscid flow and $M_\infty = 3.0$, $\alpha = 0.5$ deg and 8.5 deg for the viscous flow. For the Navier-Stokes case a Reynolds number $Re_{\bar{D}} = 2.30 \times 10^6$ is used, the Prandtl number is set to $Pr = 0.738$, and a fixed solid-wall temperature is assumed, with $\bar{T}_w = 292$ K, $\bar{T}_\infty = 104.29$ K. The transition laminar-turbulent is fixed at $x_{Tr} = 0.6\,\bar{D}$. The position for the laminar-turbulent transition is based on experimental information. The case $M_\infty = 3$, $\alpha = 8.5$ deg corresponds to the onflow conditions for the available oil flow picture.

For the computational grid a C-O topology is used as shown in Fig. 2. The first i-plane is degenerated to the cone's nose point. This has the advantage that the mesh is very dense in the vicinity of the attached shock. The last i-plane is used as an outflow boundary. The first and last k-planes are therefore symmetry boundaries, $y = 0$. The mesh was obtained with a two-dimensional elliptic mesh generator applied successively for planes in the axial direction.[17]

The generated mesh had 113 × 65 × 225 points for the Navier-Stokes case and 77 × 41 × 225 points for the Euler case. It was checked that the distribution of y^+ for the first point away from the wall, which is a measure of near-wall grid resolution, was less than 1.0 over the complete surface. The variable y^+ is the dimensionless wall distance and expressed as $y^+ = \sqrt{\rho_w \tau_w} d/\mu_w$, with d being the distance to the wall and

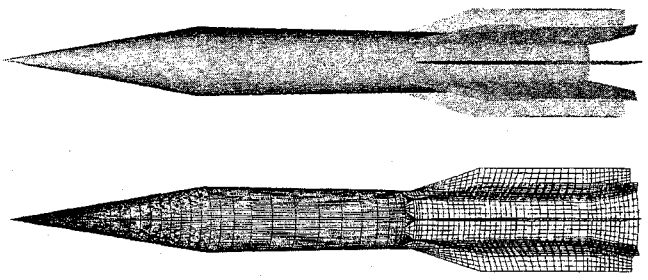

Fig. 1 Configuration and surface mesh for Euler solution (only each fourth mesh line shown in spanwise direction).

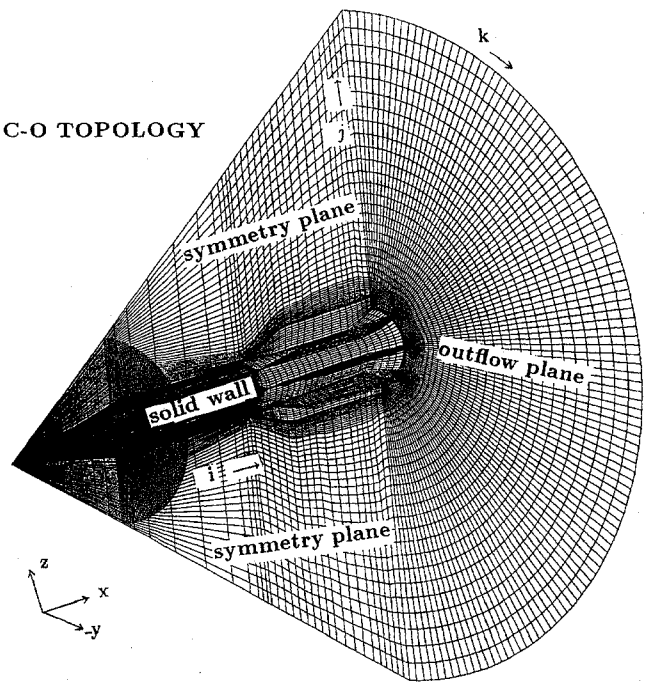

Fig. 2 C-O topology for computational grid.

τ_w being the wall shear stress. For the flow solver these grids are blocked with five-blocks in the axial direction for the Euler case and 12 blocks for the Navier-Stokes case (four times in the spanwise direction and three times in the axial direction).

Convergence to Steady State and Grid Convergence

For the Euler solutions the reduction of the residuum for the continuum equation was used as the criteria of convergence to the steady state. The grid averaged root mean square of $\partial\rho/\partial t$ was reduced between four and five orders of magnitude in 300 iterations.

For the Navier-Stokes solutions convergence was accelerated using four multigrid levels.

Figure 3a shows the convergence history for the forebody. The solution was started with the freestream condition at the coarsest level and after convergence it was interpolated down to the next-finest level. This procedure was repeated until the finest level was reached. The residuum is reduced by four orders of magnitude. The CPU time needed to execute one multigrid cycle for one grid point is about 100 μs on a single Cray Y-MP processor. For the finned afterbody of the projectile, the residuum was also reduced by four orders of magnitude. For the afterbody the solution did not converge any further; the residuum stalls at the outflow boundary.

Figure 3b shows the grid convergence for the normal-force and pitching-moment coefficients. The difference between the values for the two finest mesh levels is less then 1%. In addition, note that for this flow case the steady value is already obtained after about 120 iterations.

In Fig. 4 the wall streamlines for the finned afterbody are shown for the solutions obtained on the finest and next-coarsest mesh. In going from the coarse to the fine mesh solution no additional flow features appear. This indicates that further grid refinement is not necessary.

Global Force and Moment Coefficients

The normal-force, pitching-moment, and drag coefficients obtained from the Euler solution and Navier-Stokes solution are compared with the experimental data for $M_\infty = 3.0$ in Fig. 5. $S_{ref} = \pi D^2/4$ is used as a reference area. Moments are referenced to a coordinate system placed at the base center using D as the reference length. For the inviscid solution the numerical values for normal force and moment show small discrepancies with the experimental values. This small discrepancy is also observed for the $M_\infty = 4.25$ results not shown here.

A more sensitive comparison between numerical and experimental values is given in Fig. 5d which shows the position of the aerodynamic center. The aerodynamic center is defined as the moment reference point with a vanishing pitching moment and therefore gives valuable information for the longitudinal stability. It is given by $x_l/D = -C_{mb}/C_{zb}$. In this case when $\alpha = 0$ deg, C_{mb} and C_{zb} vanish. A Taylor series for x_l, around $\alpha = 0$ deg then results in

$$x_l = -\left(\frac{\partial C_{mb}/\partial\alpha}{\partial C_{zb}/\partial\alpha}\right)D \tag{13}$$

The numerical and experimental position of the aerodynamic center differs by less then 1/10th (1/6th) caliber for $M_\infty = 3.0$ ($M_\infty = 4.25$), so that for this quantity the Euler solution provides a sufficiently accurate value.

Surprisingly, a comparison between the Euler and Navier-Stokes solution, for $M_\infty = 3.0$, $\alpha = 8.5$ deg, concerning the normal-force and moment coefficients shows a relative discrepancy which is less then 1%. However, if the surface contributions from the forebody and finned afterbody are considered separately large relative differences are found for the normal-force (moment) coefficient with opposite signs for the forebody and afterbody sections (see Table 1).

As expected for this type of configuration the shear stress has a large contribution to the drag coefficient. Therefore, the inviscid drag amounts only to 60% of the total measured C_{xa}.

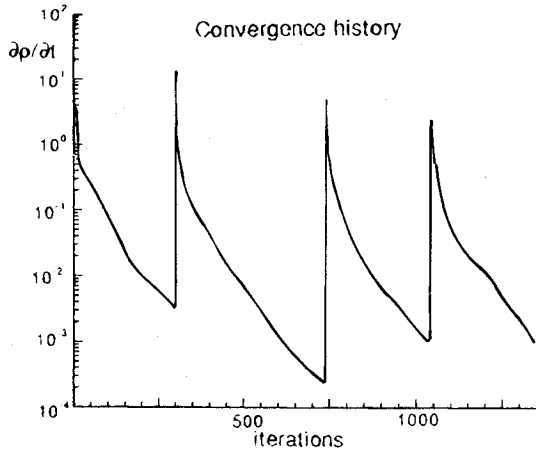

a)

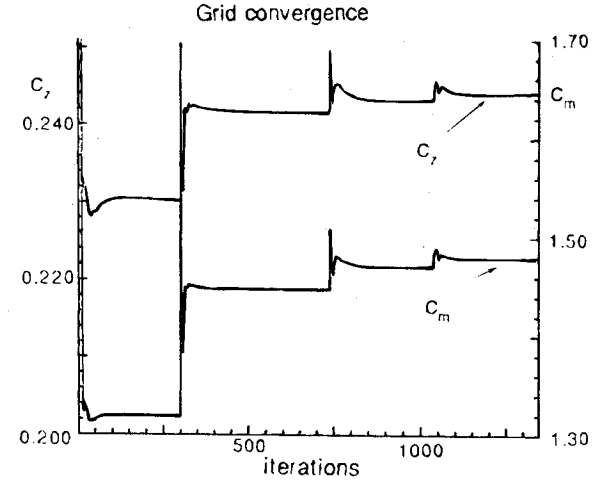

b)

Fig. 3 Convergence for the Navier-Stokes solution, $M_\infty = 3.0$, $\alpha = 8.5$ deg: a) convergence history (forebody) and b) grid convergence and convergence history for normal-force and pitching moment (forebody).

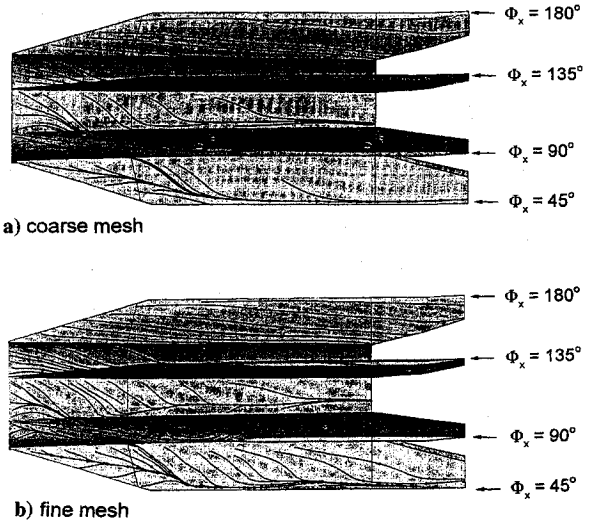

a) coarse mesh

b) fine mesh

Fig. 4 Grid convergence for finned afterbody, Navier-Stokes solution, $M_\infty = 3.0$, $\alpha = 8.5$ deg: to see the flow on the leeside of the fins, the body has been rotated by 60 deg towards the windward symmetry plane (placed at 0 deg).

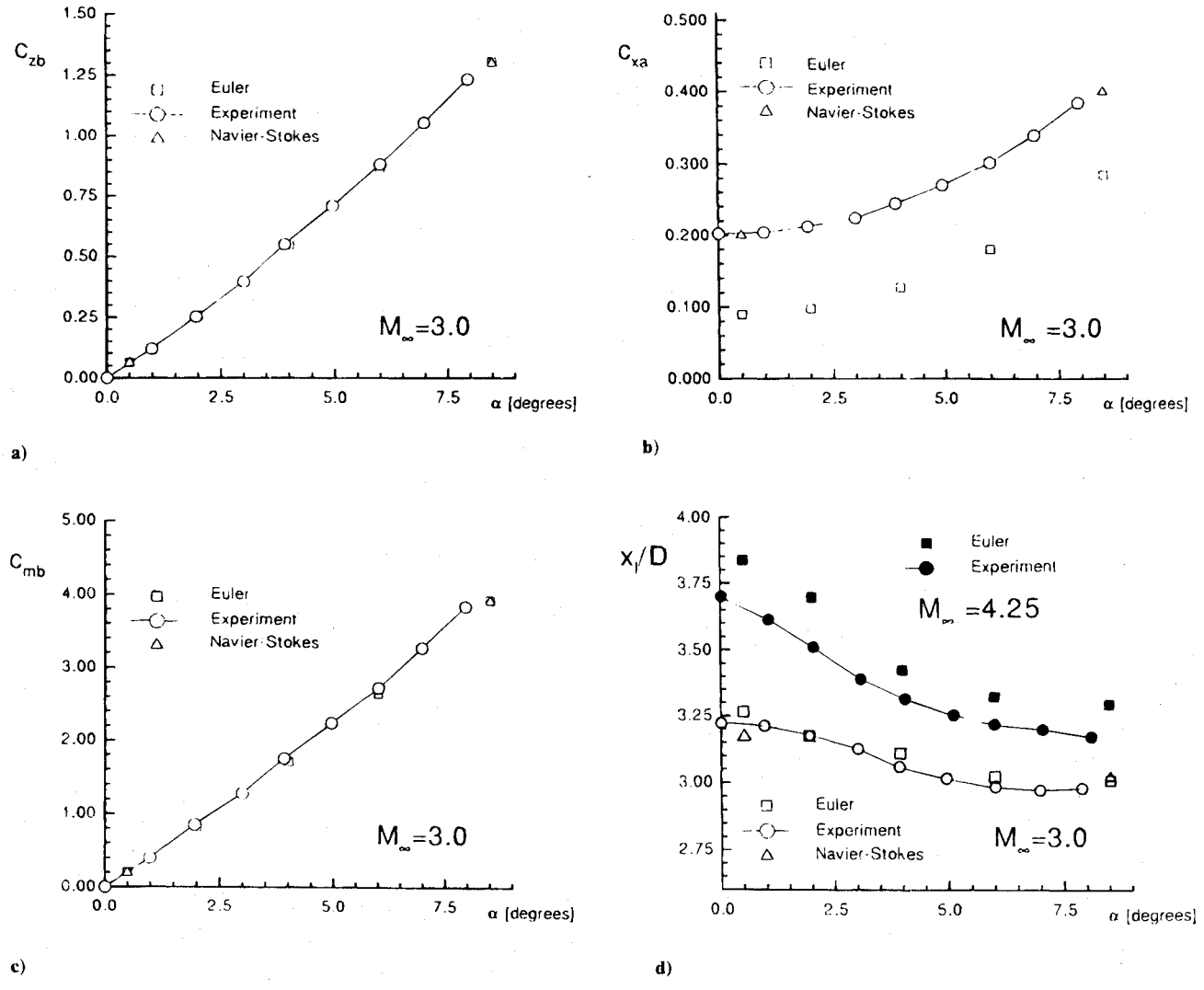

Fig. 5 Global aerodynamic coefficients: a) normal-force, b) pitching-moment, c) drag cofficient (without base drag), and d) aerodynamic center as function of Mach number and angle of attack with position measured from the base.

Table 1 Relative difference (in %)c_{inv}/c_{vis} for M_∞ = 3.0, α = 8.5 deg[a]

Surface section	C_{zb} Δ(%)	C_{mb} Δ(%)	C_{xb} Δ(%)
Forebody	6.4	5.60	41.01
Tail (fins)	−3.1	−16.11	86.40
Total	0.5	0.18	55.82

[a]With $\Delta = 1 - c_{inv}/c_{vis}$.

To compare with the experimental results the contribution from the base has been subtracted from the experimental drag coefficient. As a first approximation for the base pressure the estimated experimental C_p^{Base} values [−0.0913 (−0.0432) for M_∞ = 3.0 (M_∞ = 4.25) at α = 0 deg] were taken. Fig. 5b shows a good agreement with the experimental values obtained for the total drag Navier-Stokes results.

Flowfield

The flowfield will be described by using contour plots at selected planes. Discussions concentrate on the flow condition M_∞ = 3.0 and α = 8.5 deg since the most complete numerical and experimental information is available for this case. Except for the boundary layer region, the flowfield obtained by the Euler and Navier-Stokes solution is very similar.

Figure 6a shows the isomach lines for the symmetry plane. The attached shock at the nose, an expansion fan at the intersection of both conical sections, and a shock at the windward side in the fin region were observed. These flow properties are recognized as well in the Schlieren picture, shown in Fig. 6b. The large fin number leads to a complicated flow in the rear part. To describe the flow in the finned region the isobars for several crossflow planes are shown in Fig. 7. Shocks arising at the windward side of the fins leading edge move down, first along the body and then through the leeward flow of the next lower fin. An interaction with the leeside crossflow shocks of the lower fin takes place. In particular, one can identify the shock described earlier in the rear part of the symmetry plane (Figs. 6a and 6b). A comparison of the inviscid flow solution with the viscous one does not show significant differences for the outer flowfield.

Surface Streamlines and Vortex Topology

The oil flow picture is compared with the numerical results for the surface. First the solution for the forebody is considered. Since the angle of attack is not large (8.5 deg), only a weak crossflow separation is expected for the smooth surface of the forebody. The oil flow picture shows a separation line on the rear conical section of the body (see Fig. 8a). Despite the fact that the inviscid solution shows a crossflow shock on the rear part of the forebody surface, this does not induce a crossflow

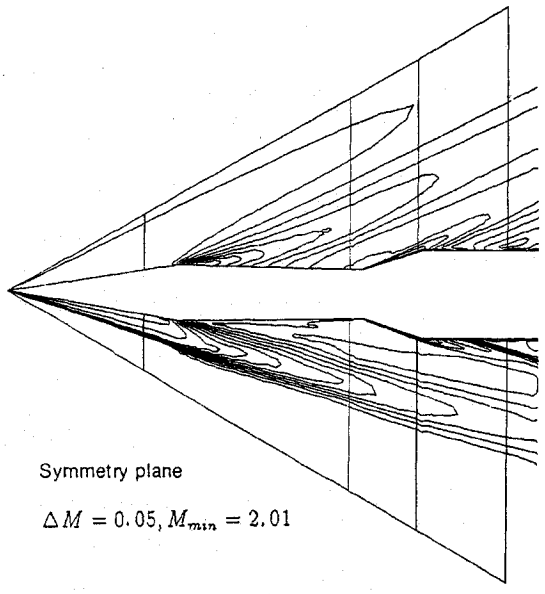

a)

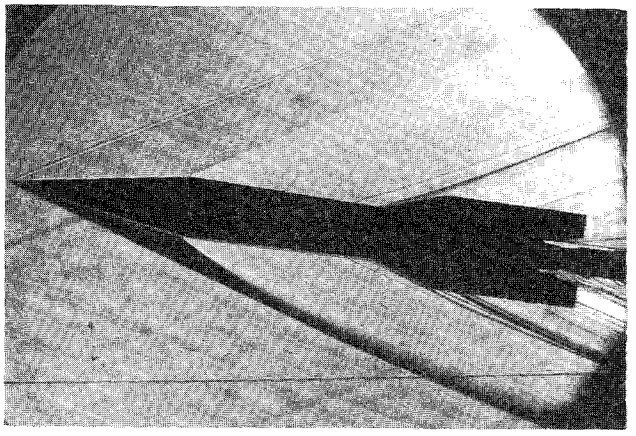

b)

Fig. 6 Flowfield for $M_\infty = 3.0$, $\alpha = 8.5$ deg: a) Euler solution: isomach lines for the symmetry plane, and b) Schlieren picture.

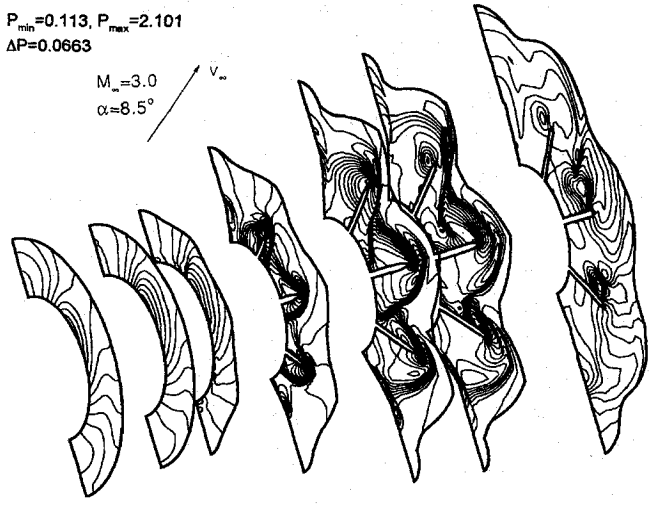

Fig. 7 Isobares for crossflow planes in finned region, Euler solution $M_\infty = 3.0$, $\alpha = 8.5$ deg.

separation. In contrast, Fig. 8b shows the viscous result for the forebody which features a separation line. The comparison with the position of the separation line observed experimentally shows good agreement with the numerical Navier-Stokes result. The associated vortex is seen in Fig. 8c, which shows the streamlines for a crossflow plane section at $x/L = 0.647$.

Figure 9 shows a comparison between experimental, Euler, and Navier-Stokes results for the surface of the finned afterbody. The uppermost fin shown in Figs. 9a–9c corresponds to the fin lying in the symmetry plane, at the leeward side. To see the flow on the leeside of the fins the body has been rotated by 60 deg towards the windward symmetry plane. The comparison of the skin friction lines of the oil flow (Fig. 9a) and the streamlines of the inviscid result (Fig. 9b) shows large differences. This is expected since the inviscid result for the flow upstream of the fins is already different as was shown previously. The separation lines seen in the oil flow picture are missing in the inviscid result. In contrast, the viscous result shows a series of separation lines on the body and fins, which can be identified as well on the oil flow picture. There are some differences in their position, especially at the lowest fin shown. A dark line is seen in the oil picture flow on this fin which does not appear as separation line for the Navier-Stokes solution. This line may be attributed to the crossflow shock on

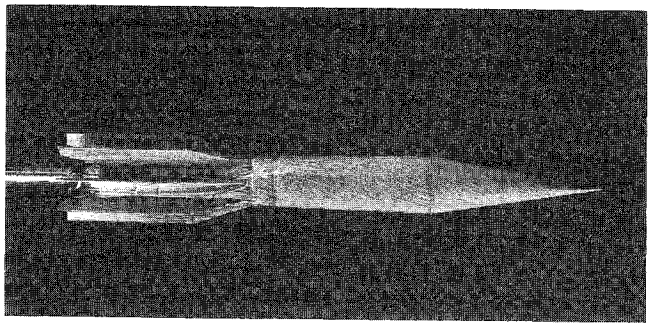

a)

b)

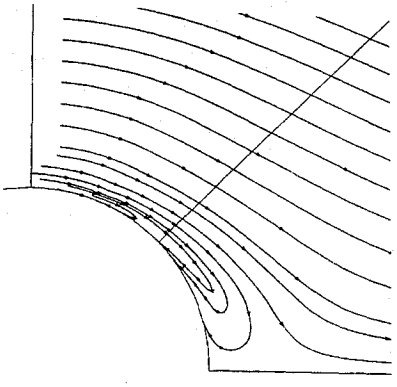

c)

Fig. 8 Forebody flow separation for $M_\infty = 3.0$, $\alpha = 8.5$ deg: a) oil flow picture, b) wall streamlines obtained with Navier-Stokes solution (the experimental separation line is indicated with a dashed line), and c) associated vortex at crossflow plane with $x/L = 0.647$.

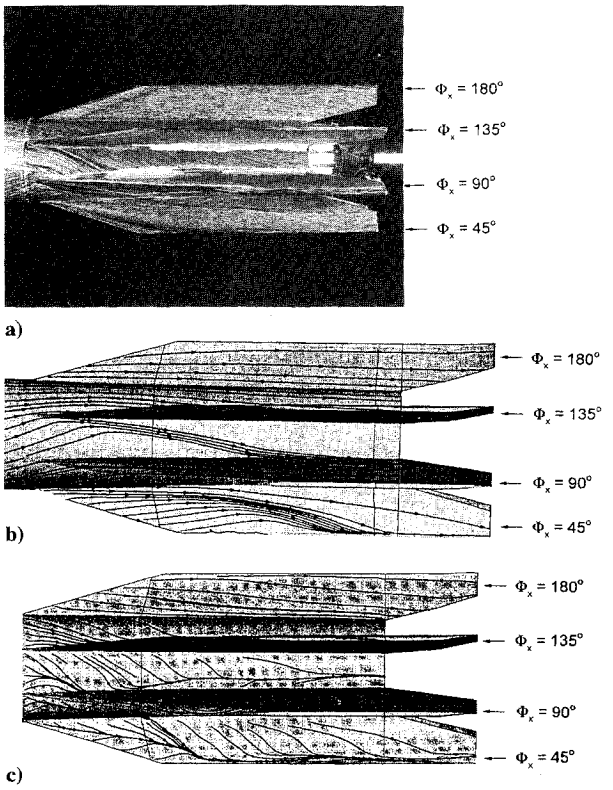

Fig. 9 Comparison between experimental, Euler, and Navier-Stokes results for the surface of the finned afterbody, $M_\infty = 3.0$, $\alpha = 8.5$ deg.

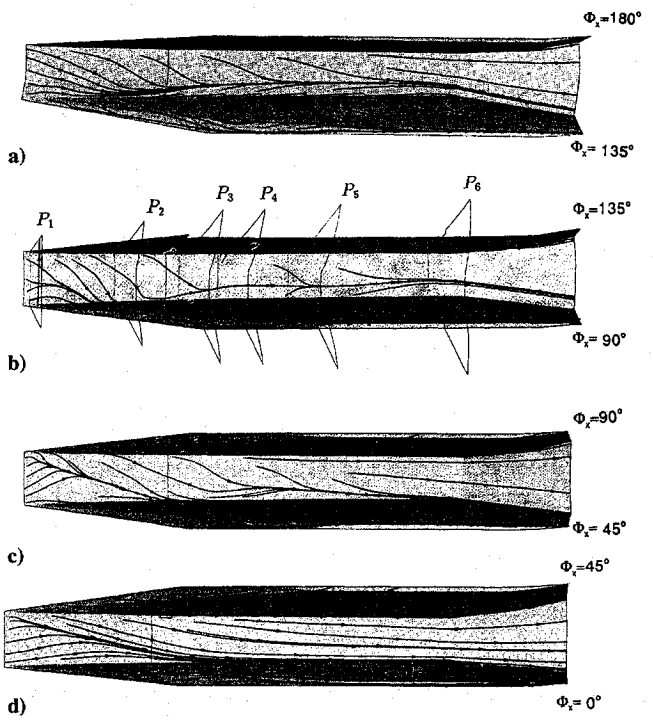

Fig. 10 Wall streamlines for the finned afterbody; Navier-Stokes solution $M_\infty = 3.0$, $\alpha = 8.5$ deg: a) section with 135 deg $< \Phi_x <$ 180 deg, b) section with 90 deg $< \Phi_x <$ 135 deg, c) section with 45 deg $< \Phi_x <$ 90 deg, and d) section with 0 deg $< \Phi_x <$ 45 deg, 0 deg corresponds to the windward side and 180 deg corresponds to the leeward side.

this fin, which occurs at nearly the same position as the dark line. In the aft region the experiment shows the streamlines turning toward the overhanging edge of the fin as expected. This is not observed in the numerical result. For the numerical computations the mesh between the overhanging fins is defined with a conical surface centerbody, as shown in Fig. 1. This surface segment is treated as an supersonic outflow boundary. This leads to the discrepancies between the numerical and experimental results. Assuming freestream conditions on the conical surface centerbody, the region of influence for this perturbation would be restricted by Mach conoids placed on the body at the base with the half angle 19.47 deg.

To analyze the separation phenomena and vortex topology in the finned region, the flow is spanwise divided in the four 45 deg sections with corresponding wall surface limited by the fins leading edge. Figure 10 shows the surface streamlines for these sections. Only the viscous solution is discussed here. The angle is measured from the windward symmetry plane $\Phi_x = 0$ deg to the leeward symmetry plane $\Phi_x = 180$ deg. In Fig. 11 transversal streamlines are shown for crossflow planes placed as indicated in Fig. 10b, for the 90 deg $< \Phi_x <$ 135 deg section. On the body the separation line coming from the forbody moves towards the lower fin (Fig. 10b). The corresponding primary vortex is seen in Fig. 11a. The inlet for the lower fin also shows flow separation with a vortex placed close to the surface. On the fin surface (Fig. 10b) one identifies the associated separation line, moving along the fin close to the leading edge. The two vortices of Fig. 11a are more clearly identified further downstream (Fig. 11b). An attachment line is also identified for the upper fin. In Fig. 11c these two vortices have merged to one vortex with the core placed over the lower fin and moving away from the body, as seen in Figs. 11d and 11e. Fig. 10b shows a third separation line on the surface which is placed on the conical body near the intersection with the lower fin. A secondary vortex can be identified for this region (see inlets for Figs. 11d and 11e). This vortex is restricted to a small domain close to the surface. The corresponding attachment line is placed on the surface of the fin, close to the intersection of the fin with the body (see Figs. 11d and 11e).

At the rear part of the afterbody the vortex topology for the sections with 45 deg $< \Phi_x <$ 90 deg and 135 deg $< \Phi_x <$ 180 deg is similar to those previous described. This is indicated by comparing the wall streamlines shown in Fig. 10a and Fig. 10c with Fig. 10b. For the section placed at the windward side (Fig. 10d) a separation line moves along the body from the leading edge of the fin placed at 45 deg towards the fin placed at the symmetry plane. The evolution of the associated vortex results in a vortex core finally placed in front of the surface of the 0 deg fin.

Surface Pressure Distribution

Figure 12a compares the Euler, Navier-Stokes, and experimental results for the pressure distribution at $x/L = 0.672$ for $M_\infty = 3.0$ and $\alpha = 8.5$ deg. C_p is plotted as a function of the angle around the longitudinal axis, Φ_x, measured from the windward symmetry plane. At this x-position which is just ahead of the fins, the experimental and viscous results mentioned earlier show a crossflow separation. In Fig. 12a one sees that the Euler and Navier-Stokes solution agree up to an angle of about 105 deg, then the inviscid flow result expands further and shows a stronger crossflow shock than the viscous one. This difference is due to the absence of the boundary layer. The agreement with the experimental results is much better for the viscous result.

Figure 12b shows the surface pressure distribution results at $x/L = 0.9$. The large peaks seen in Fig. 12b correspond to the fins whose surface as function of Φ_x is poorly resolved. However a plot of C_p against Φ_x was chosen, since the probes were placed on the conical section of the afterbody. Again, the discrepancies between experimental and numerical results are smaller for the Navier-Stokes solution. Note that there exists recompression on the body between 45 deg $\leq \Phi_x \leq$ 90 deg and between 90 deg $\leq \Phi_x \leq$ 135 deg for the viscous flow solution. These recompressions are not observed in the inviscid solution. The

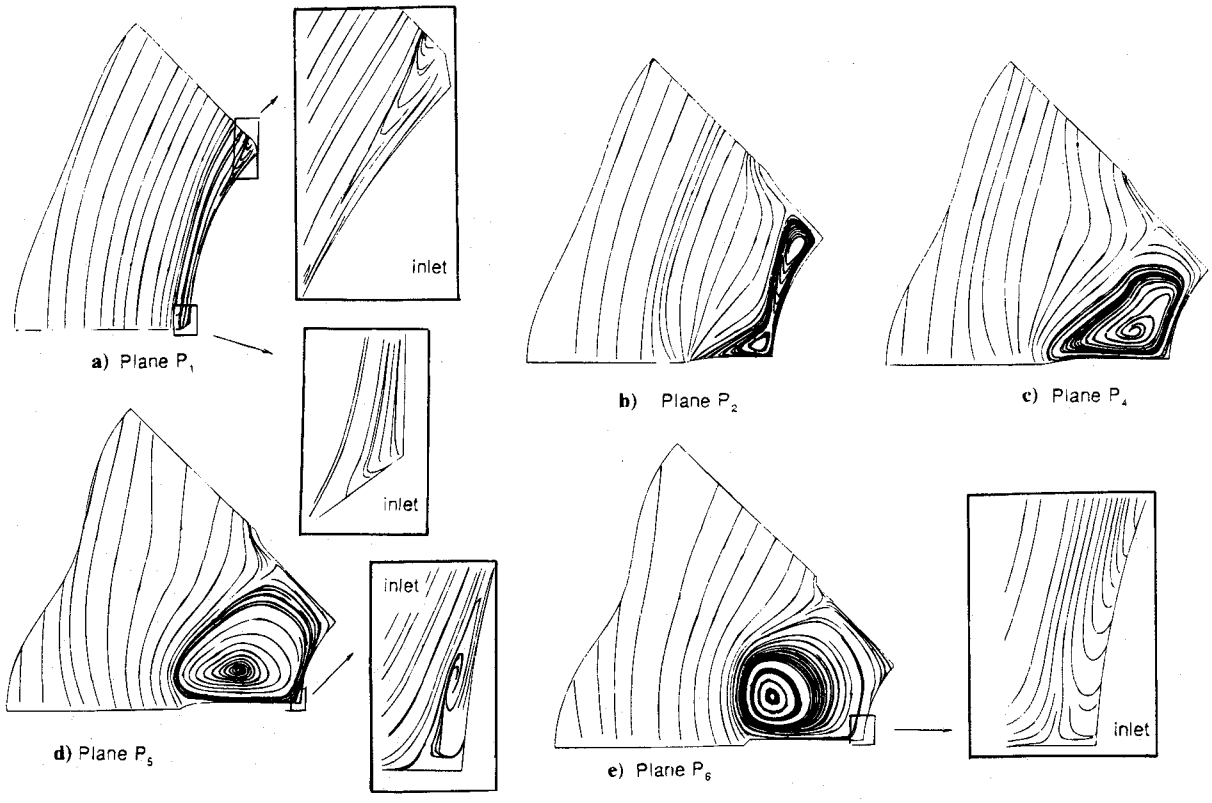

Fig. 11 Streamlines for crossflow planes with 90 deg $< \Phi_x <$ 135 deg, $M_\infty = 3.0$, $\alpha = 8.5$ deg; planes P_1 through P_6 as indicated in Fig. 10b.

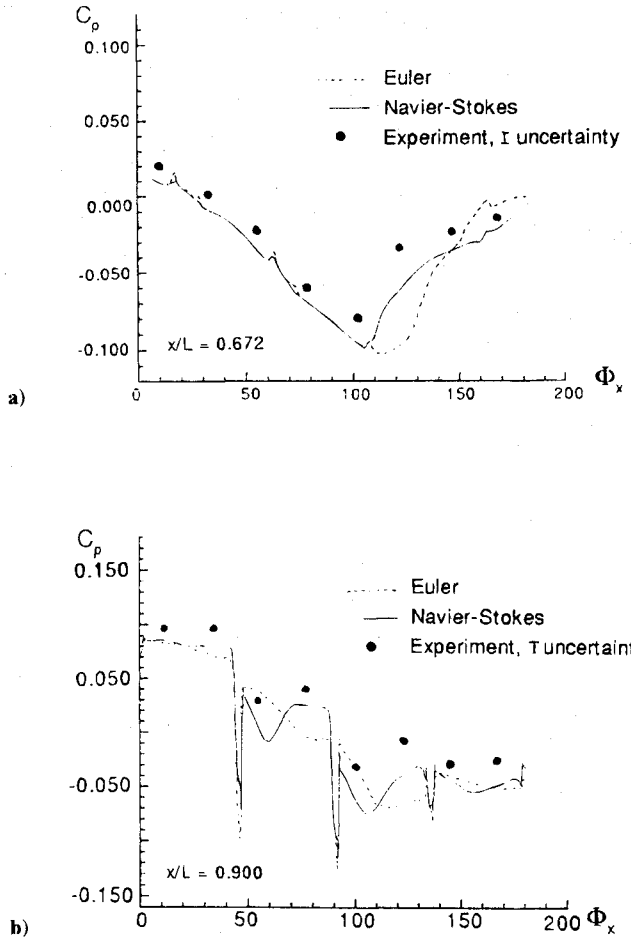

Fig. 12 Surface pressure distribution for $M_\infty = 3.0$, $\alpha = 8.5$ deg: a) at $x/L = 0.672$ and b) at $x/L = 0.9$.

pressure measurements for the rotated wall pressure orifices lead to C_p values differing by an amount ranging up to 0.0095. This value may be taken as an indication of the experimental uncertainty.

Conclusions

The inviscid and viscous flow around a complex missile with supersonic freestream conditions was computed and compared with experimental results. The configuration is a projectile with eight fins placed at the rear assembly. Freestream conditions are $M_\infty = 3.0$, 4.25 with $\alpha \leq 8.5$ deg. The numerical solution is obtained using the DLR code CEVCATS which includes several acceleration techniques especially adapted to high-speed flows.

The comparison of the inviscid result with the experimental data for the global normal-force and pitching-moment coefficients gives good agreement. Therefore the position of the aerodynamic center can be predicted up to 1/10th caliber for $M_\infty = 3.0$ and up to 1/6th caliber for $M_\infty = 4.25$. A comparison with the viscous result for $M_\infty = 3.0$, $\alpha = 8.5$ deg shows discrepancies which are less then 1%. However, if the missile is divided into afterbody and forebody, the coefficients corresponding to these sections show much larger differences. The total drag has a large contribution coming from the shear stress. Without taking into account the contribution from the base, the shear stress contribution to the total drag amounts to 40%.

The resulting flowfield shows several nonlinear features. At $\alpha = 8.5$ deg crossflow shocks and induced vortices are observed at the leeside of the smooth forebody and at the fins.

While the outer flowfield for the inviscid and viscous solution is very similar, the flow near to the surface shows large differences. The comparison with the experimental surface pressure distributions at two crossflow sections shows a better agreement with the viscous result. For the surface streamlines the viscous result shows separation lines on the smooth surface of the forebody and at the surface of the fins, which agree well with the experimental oil flow picture. These lines are not obtained for the Euler solution. The primary and secondary vortices

associated with these separation lines are identified in the flowfield. By changing from coarse- to fine-mesh solution there are no additional features for the surface flow. To validate the numerical results concerning the vortex topology and the turbulence model used here more detailed experiments are required for the flowfield in the afterbody section.

In summary it was found that the global aerodynamic coefficients are predicted by the Euler code with sufficient accuracy (excepting the drag coefficient). The reason is that the properties of the outer flowfield are well-described by assuming inviscid flow. However for the flow close to the surface a Navier-Stokes solution is required to obtain agreement with the experimental results.

Acknowledgments

I am very grateful to the Rheinmetall GmbH for enabling the present CFD study through a joint project with the DLR. I would also like to acknowledge the valuable cooperation of Helmut Esch from the DLR-TMK wind tunnel in supplying and discussing the experimental results for this flow case. To Rolf Radespiel I want to express my gratitude for the useful discussions concerning the hypersonic flow code and its acceleration techniques.

References

[1] Guillen, P., and Lordon, J., "Numerical Simulation of Separated Supersonic Flows Around Tactical Missile Bodies," AGARD Paper 88-CP-437, May 1988.

[2] Pagan, D., Molton, P., and Délery, J., "Basic Experiment on a Superscript Vortex Flow around a Missile Body," *AIAA Journal,* Vol. 29, No. 3, 1992, pp. 373–378.

[3] Lordon, J., Faré, J., and Pagan, D., "Supersonic Vortex Flows around a Missile Body: Basic Experiment and Euler Numerical Computation," AGARD Paper 15-CP-493, April 1990.

[4] Priolo, F. J., and Wardlaw, A. B., "Supersonic Tactical Missile Computations: Using Euler Equations with Crossflow Separation Modelling," AGARD Paper 6-CP-493, April 1990.

[5] Jones, D. J., Evans, J., Priolo, F., Sturek, W., and Wardlaw, A. B., "Applications of Euler and Navier-Stokes Codes to Missile Type Bodies with High L/D Ratios," AGARD Paper 8-CP-493, April 1990.

[6] Deese, J., Agarwal, R., and Gielda, T., "Computations of Supersonic Viscous Flow About Missiles and Bodies at High Angles of Attack using PNS and Navier-Stokes Solvers," AIAA Paper 89-0527, Jan. 1989.

[7] Thomas, J. L., and Hartwich, P. M., "Navier-Stokes Analysis of Flows over slender Airfraimes," *Tactical Missile Aerodynamics: Prediction Methodology,* edited by M. R. Mendenhall Vol. 142, Progress in Astronautics and Aeronautics, AIAA, Washington, DC, 1992, pp. 561–637.

[8] Radespiel, R., Poirier, D., and Streit, Th., "Computation of Viscous Flows Around HERMES (1.0) at M = 10," Deutsche Forschungsanstalt fur Luft and Raumfahrt Rept. IB 129-92/3, Institute of Design Aerodynamics, Braunschweig, Germany, March 1992.

[9] Baldwin, B. S., and Lomax, H., "Thin Layer Approximation and Algebraic Model for Separated Turbulent Flows," AIAA Paper 78–257, AIAA 27th Aerospace Sciences Meeting, Reno, Nevada, Jan. 1978.

[10] Degani, D., and Schiff, L., "Computations of Turbulent Supersonic Flows around Pointed Bodies Having Crossflow Separation," *Journal of Computational Physics,* Vol. 66, No. 1, 1986, pp. 173–196.

[11] Radespiel, R., Rossow, C., and Swanson, R., "An Efficient Cell-Vertex Multigrid Scheme for the Three-Dimensional Navier-Stokes Equations," *AIAA Journal,* Vol. 28, No. 8, 1990, pp. 1464–1472.

[12] Yee, H. C., and Harten, A., "Implicit TVD Schemes for Hyperbolic Conservation Laws in Curvilinear Coordinates," *AIAA Journal,* Vol. 25, No. 2, 1987, pp. 266–274.

[13] Schöne, J., Streit, T. S. J., and Kroll, N., "Steps Towards an Efficient and Accurate Method Solving the Euler Equations for a Re-entry Configuration at Super- and Hypersonic Speed," *Proceedings of the First European Symposium on Aerothermodynamics for Space Vehicles,* European Space Agency Publications, ESTEC, Noordwijk, The Netherlands, July 1991, pp. 115–120, ESA SP-318.

[14] Radespiel, R., and Swanson, R., "Progress with Multigrid Schemes for Hypersonic Flow Problems," Institute for Computer Applications in Science and Engineering Rept. No. 91-89, Hampton, VA, Dec. 1991; see *Journal of Computational Physics (to be published).*

[15] Radespiel, R., and Kroll, N., "Multigrid Schemes with Semicoarsening for Accurate Flow Computations of Hypersonic Viscous Flows," Deutsche Forschungsanstalt fur Luft and Raumfahrt Rept. IB 129-90/19, Institute of Design Aerodynamics, Braunschweig, Germany, April 1991.

[16] Atkins, H., "A Multi-Block Multigrid Method for the Solution of the Three Dimensional Euler and Navier-Stokes Equations," Deutsche Forschungsanstalt fur Luft und Raumfahrt Rept. FB 90-45, Institute of Design Aerodynamics, Braunschweig, Germany, Sept. 1990.

[17] Hermann, U., "An Interactive Mesh Generation Package for Graphics Super Workstations," *Proceedings of the Third International Conference on Numerical Grid Generation in Computational Fluid Dynamics and Related Fields* (Barcelona, Spain), June 1991, pp. 467–478.

Jerry M. Allen
Associate Editor